Clay Minerals (2026), **61**, 18–31
doi:10.1180/clm.2026.10022

CAMBRIDGE UNIVERSITY PRESS

Article

Geopolymer mesoporosity investigated by intrinsic ionic conductivity using complex impedance spectroscopy

Sandrine Gomes, Fabrice Leroux and Guillaume Renaudin
Université Clermont Auvergne, Clermont Auvergne INP, CNRS, ICCF, Clermont-Ferrand, France

Abstract

The precise characterization of the mesoporous mineral matrix of a geopolymer is greatly complicated by its amorphous nature. No conventional characterization technique allows for its direct investigation. We propose here the use of alternative current impedance spectroscopy (AC-IS; generally called 'complex impedance spectroscopy') as an indirect method for probing geopolymers *via* their ionic conduction properties. Our study of ∼50 K-geopolymer pellets using AC-IS has made it possible to better describe the mesoporosity of alkali-activated materials. The latter were prepared by partial substitution of metakaolin by argillite, and these were then subjected to heat treatment up to 900°C and exposed for a long time to high or low relative humidity. The metakaolin substitution rate along with post-synthesis temperature and storage conditions were the variables that allowed us to track the phenomenon of charge transport *via* mesoporosity. Refining the impedance spectra over a range of temperatures, using simple and robust models, provided a set of values for the activation energies and diffusion coefficients. The results confirmed the open and 'through-hole' nature of the porosity, the localization of K^+ cations in the interstitial liquid and their diffusion through the amorphous ceramic matrix during heat treatment, as well as the possible resumption of long-term alkaline activation for poorly reactive aluminosilicate sources.

Keywords: Alkali-activated materials; impedance spectroscopy; ionic conduction; mesoporosity

(Received 9 October 2025; revised 8 January 2026; accepted 13 January 2026)

Geopolymers – the usual name for the more conventional denomination of 'alkali aluminosilicate gels' – are inorganic solids obtained by the alkaline activation of an aluminosilicate precursor. The precursor can be either a calcined clay (usually metakaolin, a dehydroxylated natural kaolin) or low-calcium industrial aluminosilicate byproducts (e.g. fly ashes). In most cases these precursors are activated using an alkaline aqueous silicate solution based on sodium or potassium. This induces the dissolution of the precursors followed by the polymerization of $[AlO_4]^{5-}$ and $[SiO_4]^{4-}$ tetrahedra into a highly disordered three-dimensional interconnected network. The solid obtained is completely amorphous (Provis *et al.*, 2005; Duxson *et al.*, 2007a; Provis & Van Deventer, 2009; Chlique *et al.*, 2015), mesoporous (Kong *et al.*, 2007; Kriven *et al.*, 2007; Provis & Van Deventer, 2009) and presents interesting mechanical properties after setting (Palomo *et al.*, 1999; Li *et al.*, 2013). Geopolymers belong to the family of inorganic binders; however, their setting mechanism and setting products – linked to the geopolymerization reaction (Babushkin *et al.*, 1985; Xu & van Deventer 2000; Duxson *et al.*, 2007; Dimas *et al.*, 2009) – are fundamentally different from the hydration process of conventional hydraulic cements. Geopolymer binders significantly reduce CO_2 emissions compared to Portland cement production (Duxson *et al.*, 2007b; Weil *et al.*, 2009; McLellan *et al.*, 2011; Habert & Ouellet-Plamondon, 2016), present unusual thermal and acid resistance (Barbosa & MacKenzie, 2003; Fernández-Jiménez *et al.*, 2008; Pacheco-Torgal *et al.*, 2012; Li *et al.*, 2013; Malviya & Goliya, 2014), stabilize various types of waste and represent a potential solution for some radioactive wastes for which there is no other solution today (Palomo & Lopez de la Fuente, 2003; Pacheco-Torgal *et al.*, 2006; Lambertin *et al.*, 2011; Cantarel *et al.*, 2015).

Geopolymers are characterized by high thermal stability, which makes them promising candidates for various applications. Recently, an in-depth characterization of a geopolymer-type material with argillite additive formulated for a fireproof coating application (for radioactive waste containers within the framework of the Cigéo project) was carried out (Gomes *et al.*, 2020a, 2020b, 2021). Cigéo is the radioactive waste disposal facility project led by the French National Radioactive Waste Management Agency (Andra) for the long-term management of high- and intermediate-level long-lived radioactive waste. In the two first related research works, the authors emphasized the thermal stability of a model K-geopolymer matrix up to a temperature of 700°C for its mesoporous features (Gomes *et al.*, 2020a) and to 900°C for its amorphous characteristics (Gomes *et al.*, 2020b). A third contribution demonstrated the positive impact of adding an argillite filler because of its dimensional and mechanical stability at high temperatures (Gomes *et al.*, 2021). Indeed, the added Callovo-Oxfordian (COx) argillite is a natural carbonated aluminosilicate material that itself undergoes an alkaline activation reaction leading to a consolidated material, in particular due to a prior thermal activation

Corresponding author: Guillaume Renaudin;
Email: guillaume.renaudin@sigma-clermont.fr

Cite this article: Gomes S, Leroux F and Renaudin G (2026) Geopolymer mesoporosity investigated by intrinsic ionic conductivity using complex impedance spectroscopy. *Clay Minerals* **61**, 18–31. https://doi.org/10.1180/clm.2026.10022

© The Author(s), 2026. Published by Cambridge University Press on behalf of The Mineralogical Society of the United Kingdom and Ireland.

https://doi.org/10.1180/clm.2026.10022 Published online by Cambridge University Press

at 750°C (Gharzouni *et al.*, 2017; Dupuy *et al.*, 2018). The present paper completes the description of the behaviour of the mesoporous network of all of the materials formulated in this project, and in particular its variation as a function of temperature, relative humidity (RH) and ageing (characterizations and results extracted from our previous studies are therefore considered as known; the reader is invited to refer to Gomes *et al.*, 2020a, 2020b, 2021). For this purpose, a non-destructive characterization method was chosen: alternative current impedance spectroscopy (AC-IS). The data collected after scanning the materials at various frequencies and temperatures make it possible to refine their physicochemical parameters, which thus indirectly provide an understanding of the hydric properties specific to these materials that present an open and interconnected porosity.

Electrical methods have been used for more than 25 years to characterize the porous network of cementitious materials. In 2016, the review of Tang *et al.* (2016) presented the various experimental configurations (direct or alternative current, electrode contact or non-contact design, resistivity or impedance measurement) encountered in the literature. They highlighted the necessity but also the difficulty of using an equivalent electrical circuit (EEC) that exactly reproduces the behavior of the material probed and to its pore structure, as well as of being able to produce a meaningful interpretation capable of establishing a link between pore structure and diffusion properties. The importance of using an appropriate EEC model is also highlighted in the recent review by Wang *et al.* (2022) dedicated to cement-based materials. The various microstructure models used in the literature to describe all of the liquid–solid interfaces present in a concrete-type material are described there: the layer model (Gu *et al.*, 1992), the brick model (Xie *et al.*, 1993), the T and I model (Moss *et al.*, 1996), the barrier/pin-hole model (Ford *et al.*, 1997) and the conductive path models (McCarter & Garvin, 1989; McCarter, 1994; McPhee *et al.*, 1996, 1997; Cormack *et al.*, 1998; Song, 2000). The idea underlying these successive models was to implement new conductive paths specific to the microstructure of hydraulic binders: a connected pore path filled with electrolyte, a disconnected pore path, a blocked pore path, a C-S-H gel hydration product in the pore path, a C-S-H gel hydration product around unreacted cement particles and unreacted cement particles themselves (Wang *et al.*, 2022). However, the complexity of such EECs makes their modelling very uncertain and strongly brings into question the interpretation of the results obtained. This is why some authors have instead attempted to assign inherent physical interpretations to the EEC elements, such as the resistances related to different scales of ionic conduction and the admittance of constant-phase elements (CPE) attributed to electrical double layers formed at various solid–solution interfaces (Keddam *et al.*, 1997; Cabeza *et al.*, 2002, 2006; Cruz *et al.*, 2013; Dong *et al.*, 2014; Ortega *et al.*, 2015; Li *et al.*, 2016; Tang *et al.*, 2016; Chi *et al.*, 2019; Wang *et al.*, 2022). Electrical methods have mainly been used to probe the porosity of cementitious materials in order to characterize their microstructure as well as to quantify the tortuosity of their pore structures (Sanish *et al.*, 2013; Gui *et al.*, 2016; Mendes *et al.*, 2018). Other works aimed at linking electrical investigations to predictions in terms of durability (Sengul, 2014; Mendes *et al.*, 2018), mechanical resistance (Tang *et al.*, 2014; Li *et al.*, 2016; Grammatikos *et al.*, 2018; Chi *et al.*, 2019; Guo *et al.*, 2021), resistance to carbonation (Dong *et al.*, 2014), resistance to corrosion (Melara *et al.*, 2020) and the impact of the addition of nanomaterials (Da Silva *et al.*, 2021). The latter study (Da Silva *et al.*, 2021) has indicated the value of using a simple and robust EEC model to be able to link the refined electrical parameters to a physical characterization of the material, particularly to the porosity characterization (as we have done in the present study).

Among the various families of hydraulic binders, geopolymers present a much simpler pore structure, which then renders them much simpler to model. Our previous study demonstrated the diffusive and open character of the mesoporous network of a geopolymer (Gomes *et al.*, 2020a). Thus, a simple ionic conduction path, through the continuous porous network, should first be considered when interpreting the impedance measurements (Melar *et al.*, 2015; Song *et al.*, 2019; Biondi *et al.*, 2020; Liu *et al.*, 2020; Shen *et al.*, 2022). Moreover, the impedance measurements presented here were conducted on temperature cycles (78 AC-IS spectra for each sample between 243 and 313 K) to characterize the electrical phenomena according to Arrhenius laws, as previously stated (Leroux *et al.*, 2011; Melar *et al.*, 2015). This makes it possible to associate an activation energy (E_a) with the modelled electrical phenomenon without having to overinterpret the refined EEC values. The objective here is to obtain a clearer interpretation of the pore structure present in the K-geopolymer formulations (dedicated to fireproof coating applications), mainly by probing the K^+ cations and focusing on the changes observed with temperature and RH. All of the samples previously described (Gomes *et al.*, 2020a, 2020b, 2021) were scrutinized using AC-IS: from pure model K-geopolymer to 100% argillite-activated materials, from as-synthesized room-temperature samples up to 900°C post-treated samples and for samples stored at 30% and 95% RH, the entire series comprised ∼50 samples.

Materials and methods

Argillite/K-geopolymer composite synthesis, thermal treatment and storage conditions

The samples were based on the model K-geopolymers previously investigated (Gomes *et al.*, 2020a, 2020b). As a summary, the model geopolymer was obtained *via* the potassium silicate activation of a metakaolin of high purity – a non-commercial product supplied by Imerys (AGS Quarrying, F-17270 Clérac, France). Alkali-activated materials were obtained by substituting X wt.% of metakaolin by COx preheated at 750°C for 4 h (with $X = 0$, 33, 67 or 100; i.e. from pure model K-geopolymer to purely K-activated COx argillite material; see Gomes *et al.*, 2021). COx argillite was described previously (Dupuy *et al.*, 2018; Gomes *et al.*, 2021).

The samples were named XCOx-T^{RH}, with X being 0, 33, 67 or 100 of the COx argillite (750°C preheated) proportion, T being the heat treatment temperature after alkaline activation and setting (25°C, 100°C, 200°C, 450°C, 600°C or 900°C) and RH being the relative humidity of the storing conditions after heat treatment ('95' for 95% RH or '30' for 30% RH; for at least 2 months to reach equivalent equilibrium for all pellets stored at a given RH). The intent behind the two storing conditions was to vary the water-filling levels inside the porous network – from fully water saturated (XCOx-T^{95} series) to a weak filling level (XCOx-T^{30} series) – so as to produce varying behaviour in terms of ionic conduction. Note that 0COx-T^{RH} samples correspond to pure model K-geopolymers (Gomes *et al.*, 2020a, 2020b).

https://doi.org/10.1180/clm.2026.10022 Published online by Cambridge University Press

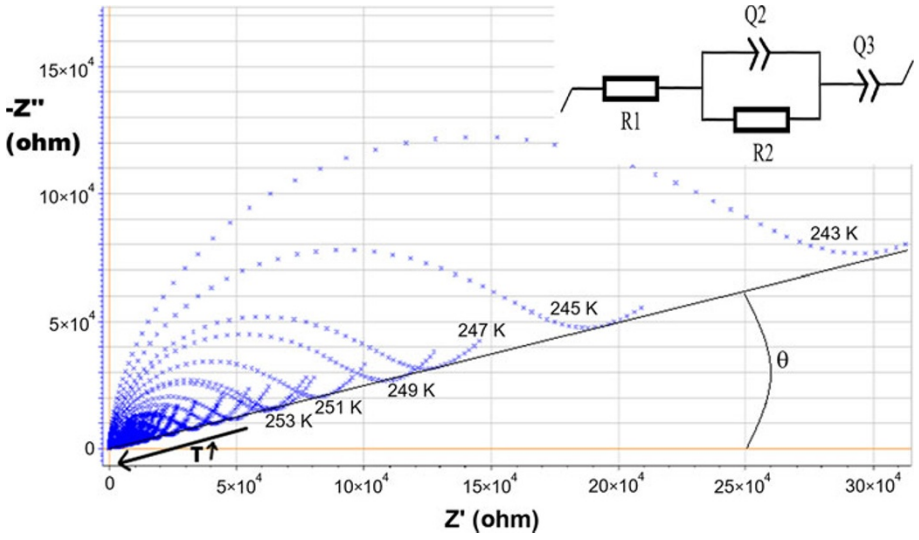


Figure 1. Nyquist representation of the 78 curves Z''–Z' (ω) for the 0COx-25^{95} pellet with the superimposition of the EEC (top right) used for the impedance modelling. The depression slope θ, related to high-frequency depleted (non-ideal) semicircles, is shown.

Alternative current impedance spectroscopy

Methods and equipment

AC-IS measurements were performed on monolithic pellets with two Au contacting electrodes in the form of a plain capacitor (14 mm diameter, between 4 and 5 mm thick). Monolithic pellets were obtained directly by demoulding after setting and hardening following alkaline activation. The cell (CESH-type sample holder controlled in temperature by the ITS chamber from BioLogic, F-38170 Seyssinet-Pariset, France) was directly wired to a 7260-type impedance analyser (Materials Mates, F-38700 Sarcenas, France) whose connectivity was customized by BioLogic. Measurements were performed over a temperature cycle ranging from 243 to 313 K in the frequency interval 10^0–10^7 Hz. The first temperature ramp was set from 293 to 243 K in steps of –2 K (ramp 1); the second ramp was from 243 to 313 K (+2 K steps; ramp 2); and the third ramp was from 313 to 293 K (–2 K steps; ramp 3). Frequency measurements were carried out with 20 acquisitions per logarithmic decade corresponding to a total of 120 points per scan. Figure 1 shows the set of 78 scans recorded for the 0COx-25^{95} sample at various temperatures.

Data processing

The impedance data were fitted using the impedance formalism defined by adopting an equivalent circuit of Ri and Qi/αi CPE. A minimum number of time constants RiCi (one in most cases) was used to reproduce the $Z' + jZ''$ spectra (i.e. the real and imaginary part of the experimental impedance Z at a given temperature). The EEC with one time constant (R1 + Q2/R2 + Q3) used in this paper is shown in Fig. 1 (top right), and Fig. S1 provides an example of the model obtained using *EC-Lab* software from BioLogic.

The total impedance was then formulated as per Equation 1:

$$Z(\mathrm{f}) = \mathrm{R1} + \frac{\mathrm{R2}}{\mathrm{R2}.\mathrm{Q2}.(j.2\pi.f)^{\alpha 2} + 1} + \frac{1}{\mathrm{Q3}.(j.2\pi.f)^{\alpha 3}} \quad (1)$$

where j is an imaginary number and f is the frequency. α2 is called the 'arc depression factor' ($0 < \alpha 2 \leq 1$; with a value of 1 for an ideal capacitor), and it is directly associated with the θ depression angle shown in Fig. 1. Both parameters refer to a non-Euclidean interface; that is to say, the ionic conduction mechanism characterized does not occur at a perfectly smooth interface. The Q3 CPE from the EEC represented in Fig. 1 corresponds to the interface between the gold electrode and the pellet that presents a purely capacitive behaviour (in agreement with the constant refined value of 1 for α3 in Equation 1; see also Da Silva *et al.*, 2021).

Activation energy

The refined R2 value was then converted to a σ conductivity value for each temperature (Equation 2, with K_c being the cell constant determined from the thickness-over-surface ratio of the pellet), and an Arrhenius plot was used assuming the following temperature-dependent behaviour for ionic conductivity (Equations 3 & 4):

$$\sigma = \frac{\mathrm{K_c}}{\mathrm{R2}} \quad (2)$$

$$\sigma.T = \sigma_0.\mathrm{e}^{\left(-\frac{E_a}{kT}\right)} \quad (3)$$

$$\log(\sigma.T) = \log(\sigma_0) - \frac{\log(\mathrm{e})\,.\,E_a}{1000\,\mathrm{k}}.\frac{1000}{T} \quad (4)$$

where T is the temperature and k is the Boltzmann constant. An example of the Arrhenius plot is shown in Fig. S2 for the two 0COx-25^{RH} pellets. The linear dependence of the plot $\log(\sigma.T)$ *vs* $1000/T$ is clearly visible, and the corresponding fitted slope (*sl*) was used to calculate the E_a related to the conduction path, in accordance with Equation 5:

$$E_a\,(\mathrm{eV}) = \frac{1000\,\mathrm{k}}{\log(\mathrm{e})}\,.\,sl = 0.1984\,.\,sl \quad (5)$$

Interestingly, a single E_a for the 0COx-25^{30} pellet stored in a dry atmosphere was obtained, whereas two were required for the 0COx-25^{95} pellet stored in a wet atmosphere (Fig. S2), indicating that a change in the physical state of the interstitial water occurred when decreasing the temperature from liquid water to solid ice (as previously observed and exploited for thermoporosimetry measurements in Gomes *et al.*, 2020a). The E_a values thus calculated will be discussed as being exclusively attributed to the K^+ alkali cations. This is obviously a simplistic view of all charge carriers participating in ionic conduction, but it is validated by a previous study that clearly attributed E_a values to the nature of the alkali used for the metakaolin activation with Na^+, K^+ or Cs^+ (Melar *et al.*, 2015).

https://doi.org/10.1180/clm.2026.10022 Published online by Cambridge University Press

Diffusion coefficient (D_{293})

The diffusion coefficient, indicating the number of charge carriers involved in the conduction mechanism being probed, was systematically determined at 293 K using the Nernst–Einstein equation (Equation 6):

$$D_{293}\,(\mathrm{cm}^2.\mathrm{s}^{-1}) = \frac{R.T.\sigma}{F^2.C} = 2.66.10^{-7}.\frac{\sigma}{C} \quad (6)$$

where C is the concentration of the charge carrier and F is Faraday's constant. In the following we assume that ionic conduction was only due to the motion of K^+ cations, and its corresponding concentrations were determined to be 7571.6 and 5531.0 mol m^{-3} in the pellets stored in dry ($C_{K^+}^{30\%\ RH}$) and wet ($C_{K^+}^{95\%\ RH}$) atmospheres, respectively, in accordance with our previous characterizations of these samples (Gomes *et al.*, 2020a, 2020b). The concentrations to be considered for these calculations are related to the overall composition relative to the quantity of water present because the Nernst–Einstein equation considers an isotropic conduction mode throughout the volume of the pellet. Thus, only two K^+ concentrations were used: one under high humidity and the other under low humidity (assuming that storing the pellets for at least 2 months under strict humidity control allows them to reach a common equilibrium and water content that clearly differentiates between RHs of 30% and 95%). Considering only alkali cations to model ionic conduction is an approximation that does not allow discussion of the absolute calculated D_{293} values but allows comparison of pellets within a series. Such a simplification of the studied system is assumed because all of the omitted ionic concentrations (major hydroxyl and minor solvated aluminate and silicate) are equivalent for all pellets stored under the same humidity conditions. Again, the aim is to describe our system using the simplest model in order to make it robust.

Surface fractal dimension (D_s)

The depression angle θ (Fig. 1), correlated to the high-frequencies-depleted semicircle, is related to the α2 exponent (from Equation 1) by Equation 7. This depression factor was linked to the fractal dimension D_s of the interface of the conduction paths within the geopolymer matrix by the empirical Equation 8 ($1 < D_s \leq 3$, D_s approaching the value of 3 for an ideal capacitor, with $\alpha 2 = 1$, with a smooth surface):

$$\alpha 2 = 1 - (2\vartheta/\pi) \quad (7)$$

$$D_s \approx 2a2 + 1 \quad (8)$$

The concept of fractal geometry used here is related to surface irregularities (more or less smooth interfaces), which was defined more than 40 years ago (Nyikos & Pajkossy, 1985), subsequently confirmed (Imre *et al.*, 1992; Massey, 1996) and used for porous media (Risovic *et al.*, 2008; Xia *et al.*, 2021). The rougher the interface (the more it deviates from a smooth surface – in other words, from a Euclidean particle), the more dispersed the ionic motion facilities and therefore the flatter the high-frequency semicircle on the measured impedance spectrum. This notion of the fractal dimension being linked to the depression factor is related to the notion of material homogeneity, and also to the tortuosity of the porosity, discussed by Da Silva et *al.* (2021).

Results

The pure model K-geopolymer: the 0COx-T^{RH} series

Cell control: reproducibility of AC-IS acquisitions (0COx-25^{95} sample)

To check the tightness of the measuring cell, and therefore to ensure a constant pellet hydration rate for the 78 recordings during the temperature cycle (between 2 and 3 days of acquisition time), and to check the reproducibility of the results, two kinds of tests were performed: (1) three successive temperature cycles on the same pellet without extracting it from the cell between the three acquisitions; and (2) three AC-IS acquisitions on triplicated equivalent pellets. These tests were performed on the 0COx-25^{95} sample.

The three successive temperature cycles performed on the same 0COx-25^{95} pellet show highly similar results. The Arrhenius plots (Fig. 2a) are perfectly superimposable and lead to similar numerical values for E_a and the diffusion coefficient (Table 1). The three E_a (liquid) values were identical (0.25 eV) for the three successive cycles, whereas a slight decrease was observed in the solid-state E_a (ice) from 1.26 to 1.22 eV. The main difference lies in the temperature at which the slope breaks during the first temperature drop ramp (ramp 1). This break in the slope corresponds to the change in the physical state of the water from liquid to ice, which is an indication of its state of confinement. The water molecules probed here constitute the pore solution; this temperature (less than 273 K) is therefore indicative of their confinement imposed by the mesoporosity (pore radius ~3 nm), but also of the chemical composition (very alkaline and K^+ concentrated; see Gomes *et al.*, 2020a). The slope break decreases from 263 K for the first cycle to 255 K for the two following ones. With the composition of the solution being invariable during these temperature cycles, it is concluded that this lowering in temperature at which the change of state occurs is due to a confinement effect, which is apparently stronger than for the first temperature cycle. We can therefore surmise that during the freezing of the interstitial solution, internal mechanical stress led to the formation of additional micro-cracks, thus shrinking the average pore size. Furthermore, the absence of a shift in the thaw temperature during ramp 2 (269 K for the three temperature cycles) is explained by confinement engendered by the mesoporosity that is assimilated to cylinders, as already demonstrated by thermoporosimetry experiments (Gomes *et al.*, 2020a). The formation of micropores does not modify the preferential ionic conduction paths through the mesoporosity and therefore does not modify the values extracted from the three temperature cycles for E_a (not at all in the liquid state, and shifted very slightly because such formation is easier in the solid state) and for the diffusion coefficient at room temperature.

The three acquisitions carried out on triplicated 0COx-25^{95} pellets (Fig. 2b) ensure reproducibility. The extracted values (Table 1) show the reproducibility of E_a as well as of the diffusion coefficient. According to these reproducibility tests, uncertainties were evaluated and fixed at ±0.02 eV for E_a in liquid, ±0.05 eV for E_a in ice and 10% uncertainty for D_{293} (uncertainties indicated here therefore correspond to the standard deviations derived from replicates).

Effect of storage relative humidity: 0COx-25^{RH} samples

Figure 2a also superimposes the same pellet preparation (0COx-25^{RH}) followed by storage in wet (95% RH) or dry (30% RH) humidity conditions for almost 2 months of equilibration before AC-IS acquisition. Two striking facts emerge from

https://doi.org/10.1180/clm.2026.10022 Published online by Cambridge University Press

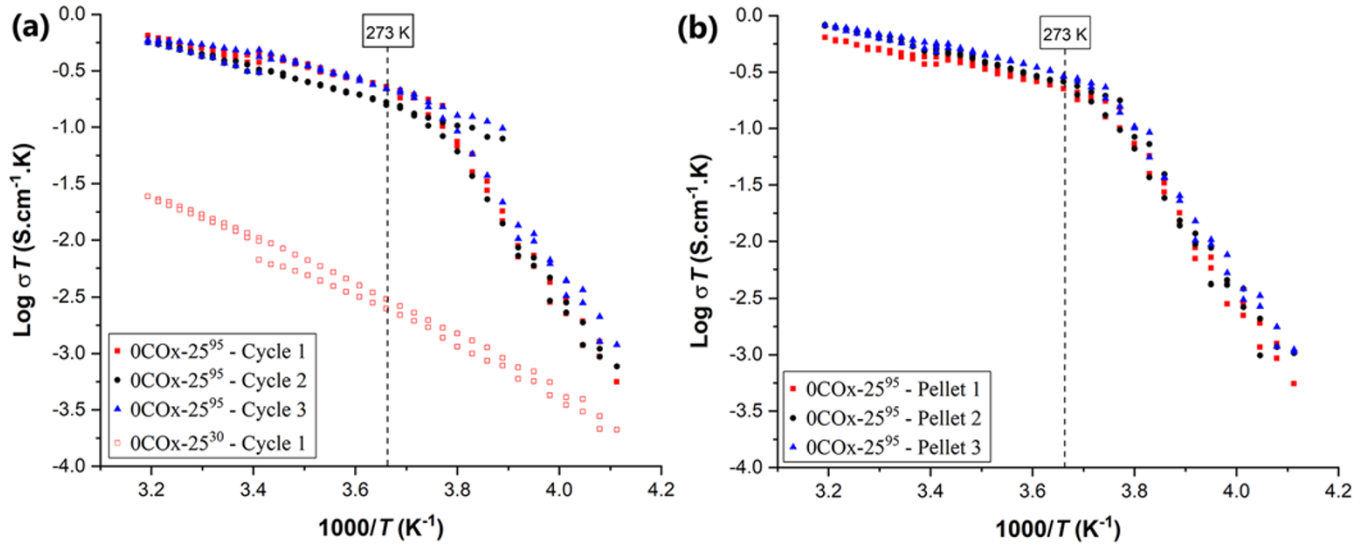


Figure 2. Arrhenius plots of the reproducibility tests: (a) three successive cycles on the same 0COx-25^{95} pellet superimposed on one cycle on a 0COx-25^{30} pellet; (b) one cycle on triplicated 0COx-25^{95} pellets.

Table 1. Values extracted from the EEC modelling of the spectra recorded on pure K-geopolymer 0COx-T^{RH} samples: E_a from the Arrhenius plot, diffusion coefficient calculated at 293 K during ramp 2 and freezing temperature for 0COx-T^{95} samples observed during ramp 1.

	E_a (eV)			
Sample	Liquid	Ice	D_{293} (cm^2 s^{-1})	T_{freeze} (K)
0COx–25^{95} pellet 1, cycle 1	0.25	1.26	0.85×10^{-7}	263
0COx–25^{95} pellet 1, cycle 2	0.25	1.21	0.76×10^{-7}	255
0COx–25^{95} pellet 1, cycle 3	0.25	1.22	0.83×10^{-7}	255
0COx–25^{95} pellet 2	0.25	1.21	0.87×10^{-7}	263
0COx–25^{95} pellet 3	0.24	1.23	0.88×10^{-7}	265
0COx–25^{30}	0.44		1.24×10^{-9}	–
0COx–100^{95}	0.20	1.22	0.83×10^{-7}	263
0COx–100^{30}	0.44		0.75×10^{-9}	–
0COx–200^{95}	0.18	1.24	0.84×10^{-7}	263
0COx–200^{30}	0.43		0.65×10^{-9}	–
0COx–450^{95}	0.18	1.05	0.79×10^{-7}	263
0COx–450^{30}	0.40		0.53×10^{-9}	–
0COx–600^{95}	0.18	1.03	0.11×10^{-7}	255
0COx–600^{30}	0.39		0.55×10^{-9}	–
0COx–900^{95}	–	–	–	–
0COx–900^{30}	–		–	–

this superimposition: (1) there is an absence of a break in the slope for sample 0COx-25^{30}; and (2) there is a lower conductivity (~10^{-3} S cm^{-1} at 95% RH and ~10^{-5} S cm^{-1} at 30% RH at room temperature). This is linked to the difference in water saturation present within the mesoporous network: from fully saturated for 0COx-25^{95}, with the liquid solution filling the pore structure, to a simple layer of physisorbed alkaline solution at the pore interface for 0COx-25^{30}. The pellets stored under low RH, with a pore network that is far from being saturated, do not show any change in the physical state of the solution (i.e. a physisorbed layer that does not transform from liquid to solid state), which is associated with a significantly lower quantity of diffusive ions (resulting in a lower diffusion coefficient). However, it should be noted that E_a remains in the same order of magnitude for the two storage conditions: 0.25 eV for 0COx-25^{95} considering the liquid phase and 0.44 eV for 0COx-25^{30}. The values obtained here are in perfect agreement with a previous study in which the nature of alkali cations was investigated: E_a for samples dried for 2 months was 0.53 eV for a Na-geopolymer, 0.46 eV for a K-geopolymer (to be compared with the value of 0.44 eV in the present study) and 0.31 eV for a Cs-geopolymer (Melar *et al.*, 2015). This reveals that the ionic conduction mechanism, through mesoporosity, should mainly be attributed to the alkaline cation and is facilitated by the saturation of the interstitial solution. Therefore, this indicates that ionic motion is mediated by a hopping mechanism *via* surface sites at the solid/liquid interface of the mesoporosity. We can thus conclude that the ions present in the pore solution, which are mainly K^+ (with the OH^- anions appearing to be secondary for the ionic conduction mechanism here), are preferentially located at this liquid/solid interface, even when the pore volume is saturated with interstitial solution. Such a similarity in the mechanism of ionic conduction under dry or wet atmospheres (i.e. under water saturation or not of the porous network) may seem counterintuitive. However, recent data from the literature provide greater understanding regarding this observation: the molecular dynamic behaviour of water molecules confined in a clay pore shows a strong increase in aqueous viscosity with decreasing pore size (Zhang *et al.*, 2025). The nanometric pore sizes measured in our samples (Gomes *et al.*, 2020a) are perfectly consistent with there being a limited number of water molecules around each solvated K^+ cation. Consequently, in this confined state (whether under low or high humidity) the ions never behave like species in solution, and their motion occurs near the solid/liquid interface *via* a hopping mechanism. Such a mechanism of ionic transport by hopping from site to site at the solid/liquid interface may represent the transposition of the electrically activated attachment/detachment model mechanism for the migration of species in strongly alkaline solutions through a porous media (Bai *et al.*, 2025a, 2025b).

The calculation of the D_s fractal dimension associated with the conduction paths indicates a relatively equivalent state of the mesopore interface whatever the capillary liquid saturation, with values of 2.56 and 2.64 (Table 2) for the 0COx-25^{30} and 0COx-25^{95}

https://doi.org/10.1180/clm.2026.10022 Published online by Cambridge University Press

Table 2. Determined depression angle θ, corresponding arc depression factor α2 and calculated D_s fractal dimension of the mesopore interface corresponding to the ionic conduction mechanism.

	30% RH			95% RH		
Sample	θ (°)	α2	D_s	θ (°)	α2	D_s
0COx–25^{RH}	20	0.78	2.56	16	0.82	2.64
0COx–100^{RH}	33	0.63	2.26	18	0.80	2.60
0COx–200^{RH}	34	0.62	2.24	23	0.74	2.48
0COx–450^{RH}	37	0.59	2.18	22	0.76	2.52
0COx–600^{RH}	35	0.61	2.22	31	0.66	2.32
33COx–25^{RH}	45	0.50	2.00	40	0.56	2.12
67COx–25^{RH}	38	0.58	2.16	33	0.63	2.26
100COx–25^{RH} @ 2 months	28	0.69	2.38	27	0.70	2.40
100COx–25^{95} @ 1 year	–	–	–	19	0.79	2.58

pellets, respectively. Such D_s values – not so far from the ideal value of 3 – indicate a relatively smooth interface, in agreement with continuous, uniform and little-disturbed ionic conduction paths. The slightly lower D_s value under low RH is then easily explained by conduction paths that are slightly disturbed by the absence of a continuous aqueous medium in the mesoporous network, in agreement with the previously mentioned higher E_a value for 0COx-25^{30}.

We can also notice in Fig. 2 that the last spectra (no. 78) at 293 K is almost equivalent to the starting spectra (no. 1; already at 293 K), as well as spectra no. 51 (still at 293 K, during ramp 2), which remains true for both storage media. This is a new indication of the airtight nature of the cell used, and this makes it possible to validate all of the 78 acquisitions carried out during the temperature cycle for each pellet. From this point on for the rest of this paper, only the points corresponding to ramp 2 (rise in temperature from 243 to 313 K) will be shown in the figures for the sake of concision and clarity. This ramp 2 was used for the Arrhenius plot of each measured pellet to determine and compare their activation energies and diffusion coefficients at 293 K.

*Effect of post-synthesis thermal treatment: 0COx-*T^{RH} *series*

All of the Arrhenius plots regarding pure K-geopolymers are shown in Fig. 3, consisting of 0COx-T^{RH} samples with post-synthesis heat treatment up to 600°C followed by dry and wet storage. Visually, the heat treatment up to 450°C does not greatly affect E_a (similar slopes) and impacts only slightly the diffusion coefficient (straight lines slightly shifted downwards). However, the measurements carried out on the samples heated to 900°C (wet and dry storage) cannot be represented in Fig. 3 because the recorded AC-IS spectra cannot be modelled by an EEC. They actually correspond to an infinite resistivity, indicating the absence of any ionic conduction paths (i.e. the closure of the 'through-hole' mesoporosity as clearly established previously by dilatometry (Gomes *et al.*, 2021) and by direct measurements using thermoporosimetry and sorption nitrogen isotherms (Gomes *et al.*, 2020a)).

Further observation of the effect of heat treatment is based on the values compared in Fig. 4a & Table 1. The activation energies change only moderately, with relatively similar variation for both storage media, showing a slight decrease in energies with temperature, indicating a facilitation of K^+ motion. Again, this confirms the identical ionic conduction mechanism, with the same K^+ charge carriers, for both physical states and both storage conditions. The facilitation of ionic displacement (indicated by the decrease in E_a) is to be compared with the decrease in the fractal dimension present at the interface associated with the involved mechanism (from 2.6 for 0COx-25^{RH} pellets to 2.2 for heat treatment at 600°C; Table 2). As observed during the three successive cycles on the same 0COx-25^{95} pellet (see 'Cell control: reproducibility of AC-IS acquisitions (0COx-25^{95} sample)' section earlier), the 0COx-600^{95} pellet shows a decrease in the freezing temperature to a value of 255 K. Again, this can be explained by the formation of micro-cracks due to the effects of the thermal treatment (inducing dimensional stress; see Gomes *et al.*, 2021). This micro-crack formation could explain the decrease in both E_a and D_s values *via* an increase in more heterogeneous conduction paths.

The variation in the diffusion coefficient is more noticeable (Fig. 4b & Table 1), especially under high RH, with a strong decrease after heat treatment at 600°C (reduced by almost 10-fold). As the mechanism is not blocked (decrease in E_a) and the porosity is not yet closed (Gomes *et al.*, 2020a), this significant drop in D^{30}_{293} indicates the loss of the main charge carriers from the mesoporous interface. It is interesting to note that even if the diffusion coefficients for dry 0COx-T^{30} geopolymers are very low, they still show a clear change, with a notable decrease up to 450°C, even though the mechanism is not hampered (decrease in E_a). It therefore seems that heat treatments generate a progressive loss of charge carriers, which leave the interstitial liquid. We can then deduce that, in humid storage, the transfer of K^+ ions to the mineral matrix is reversible up to 450°C, whereas such reversibility does not exist under dry conditions. Such a transfer of alkali cations from the mesoporous liquid to the mineral matrix, across the interface, is similar to the chemisorption and physisorption phenomena recently described for the theoretical and experimental coupling of Al^{3+} (Long *et al.*, 2025).

Variations in the interface fractal dimension also differentiate the two storage conditions (Table 2). The D_s value already decreases at 100°C for dry storage under 30% RH, showing D_s values of 2.3 for 0COx-100^{30} and then ~2.2 for 0COx-T^{30} pellets (T = 200°C, 450°C and 600°C). Under wet 95% RH storage, D_s variation is delayed, still being ~2.5 for heat treatment up to 450°C and decreasing to 2.3 only for the 0COx-600^{95} sample. This indicates a change in the interface, which becomes rougher from 100°C, with a reversible feature for temperatures up to 450°C in the case of wet storage. Both micro-crack formation and K^+ chemical transfer could be responsible for the observed decrease in D_s.

Impact of argillite loading: XCOx-T^{RH} *series with* X > 0

Effect of the added argillite filler amount: XCOx-25^{30} *samples*

As shown in Fig. 5a, a decrease in conductivity is observed under dry storage with the addition of argillite, which is confirmed by the numerical values ofD^{30}_{293} diffusion coefficients in Fig. 5d & Table 3. This observation is directly correlated with the loss of mesoporous volume that was measured previously with the addition of argillite filler (Gomes *et al.*, 2021). This highlights the fact that the alkaline activation of argillite does not lead to a mesoporous matrix. The decrease in pore volume is naturally correlated with the reduction in the part of the material corresponding to the metakaolin alkaline activation (i.e. the pure K-geopolymer part).

The case of the pure alkali-activated argillite 100COx-25^{30} sample is somewhat different. Not only do we observe a strong decrease in the diffusion coefficient but also an increase in the associated E_a (Fig. 5c & Table 3), corresponding in Fig. 5a to the rise in the slope for the 100COx-25^{30} plot compared to the other XCOx-25^{30} plots. We can therefore see here that the ionic conductivity mechanism

https://doi.org/10.1180/clm.2026.10022 Published online by Cambridge University Press

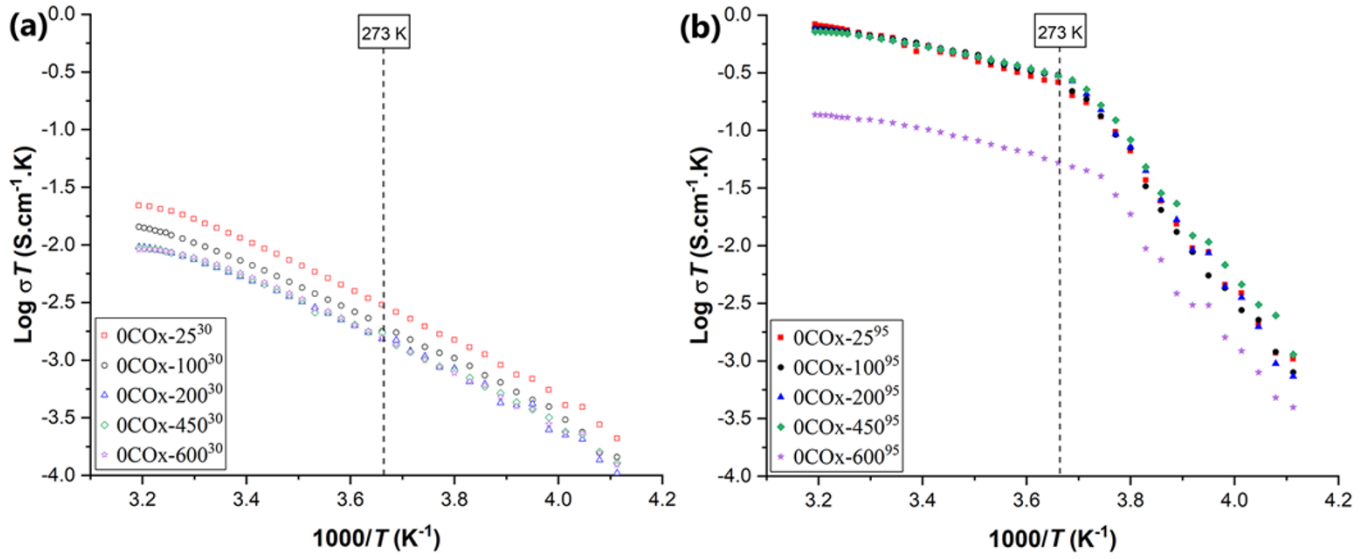


Figure 3. Superposition of the Arrhenius plots extracted from the pure K-geopolymers: (a) 0COx-T^{30} dry pellets; and (b) 0COx-T^{95} wet pellets.

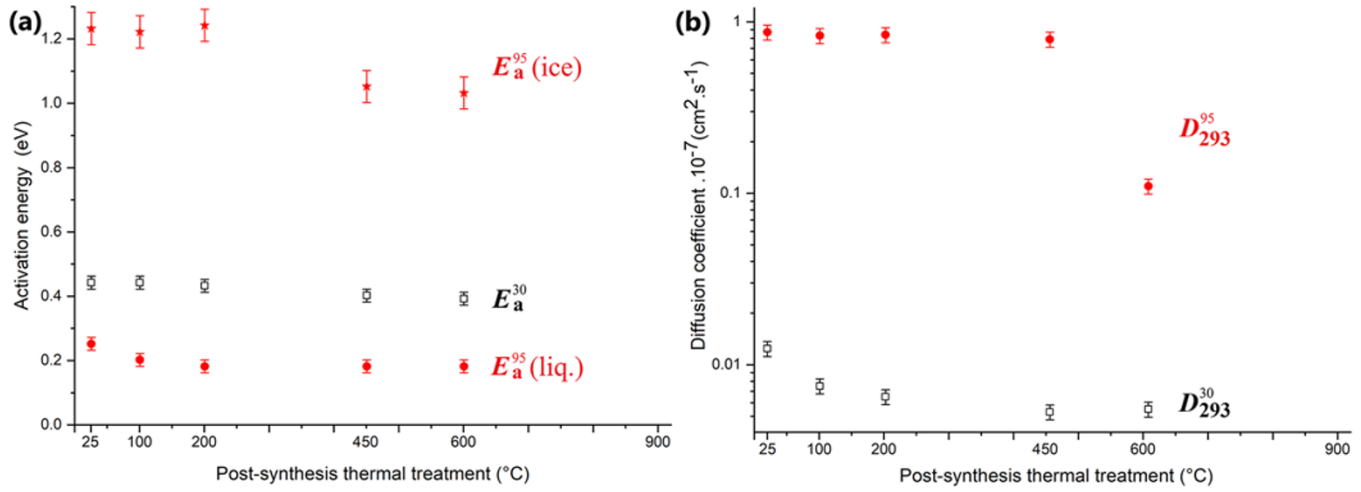


Figure 4. Variations in (a) E_a and (b) diffusion coefficient with the temperature of the post-synthesis thermal treatment for the pure K-geopolymer 0COx-T^{RH} pellets (0COx-T^{30} series in black and 0COx-T^{95} series in red). liq. = liquid.

in the materials based on the alkaline activation of the argillite is different from that corresponding to the pure geopolymer part. This new conduction path having a higher E_a of 0.67 eV for the 100COx-25^{30} sample *vs* ~0.44 eV for the pure geopolymer (Fig. 5c & Tables 1 & 3) indicates that the activated argillite inorganic framework reduces the ease of mobility for the charge carriers. Moreover, the diffusion coefficient gradually decreases with the addition of argillite filler (i.e. with the decrease in the pure geopolymer part), being three-fold less for the intermediate composite compositions of 33COx-25^{30} and 67COx-25^{30} and then by a factor of almost 10 for the 100COx-25^{30} purely argillite activated sample compared to 0COx-25^{30}. Again, the reduction by an order of magnitude for the diffusion coefficient has to be correlated with a decrease in the mesopore volume between the two 0COx-25^{RH} and 100COx-25^{RH} limit compositions (Gomes *et al.*, 2021).

Interface fractal characterization for *X*COx-25^{30} pellets (Table 2) confirmed the non-homogeneous nature of the mineral matrix upon addition of argillite. The D_s value sharply decreased to 2.0 for the 33COx-25^{30} pellet, then rose slightly to 2.2 and 2.4 for 67COx-25^{30} and 100COx-25^{30}, respectively. The value of 2.4 for the 100COx-25^{30} pellet (compared to 2.6 for 0COx-25^{30}) indicated a less ideal (i.e. less smooth) interface for argillite alkaline activation (compared to metakaolin activation). The lowest D_s values observed for the two mixed *X*COx-25^{30} (X = 33 and 67) pellets suggest the coexistence of the two poorly connected mineral subnetworks, each providing its own ionic conduction paths.

Effect of storage relative humidity: XCOx-25^{95} samples

The results from the AC-IS spectra recorded from samples stored in the 95% RH wet atmosphere show a different trend with argillite addition. Although we clearly observe the expected drop in conductivity between the 0COx-25^{95} and 33COx-25^{95} samples, we then see a clear recovery in conductivity when further increasing the amount of argillite (Fig. 5b). Sample 67COx-25^{95} is equivalent in conductivity to pure K-geopolymer, and the pure alkali-activated argillite sample 100COx-25^{95} outperforms every other sample when considering the liquid state of the interstitial solution.

https://doi.org/10.1180/clm.2026.10022 Published online by Cambridge University Press

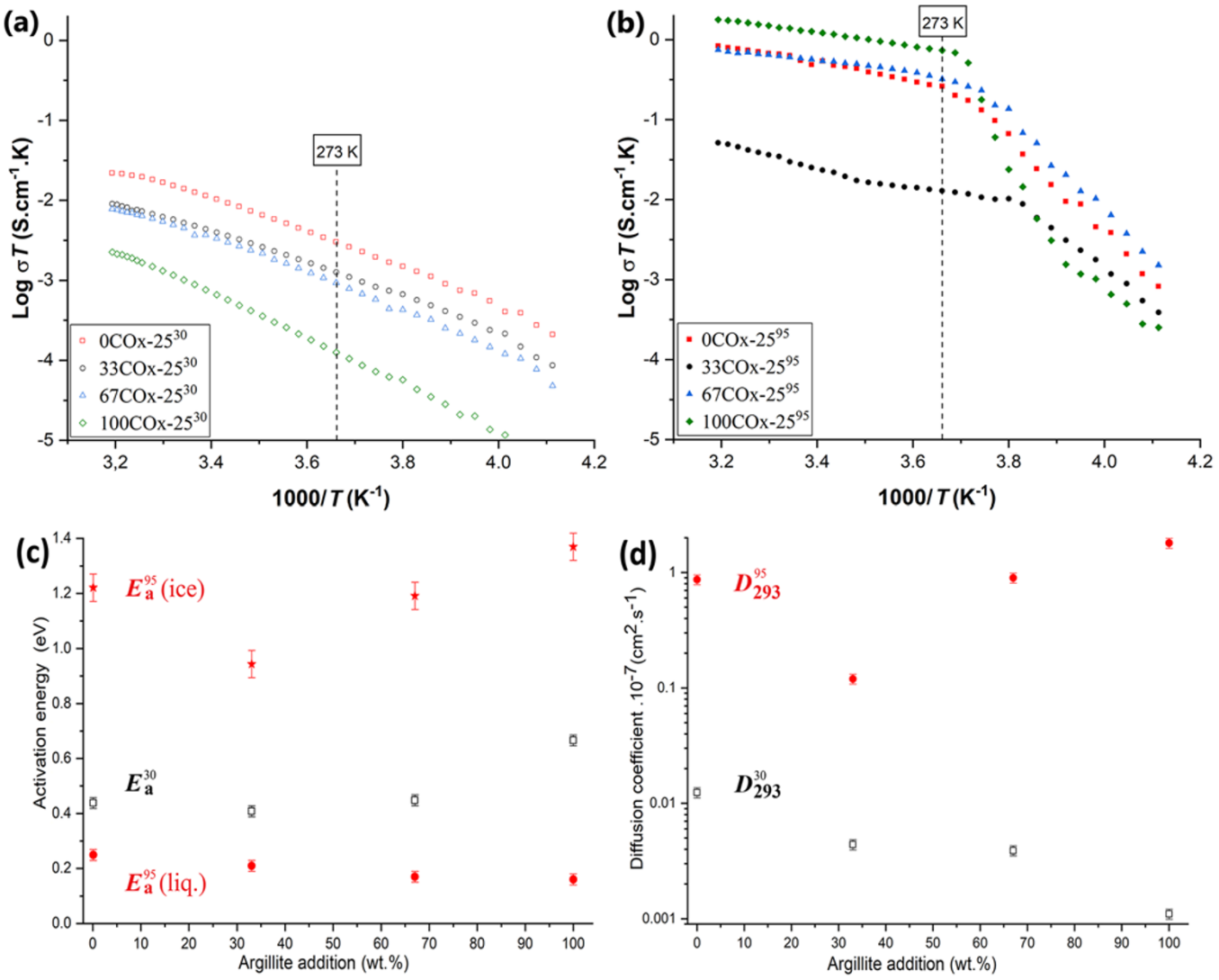


Figure 5. Superposition of the Arrhenius plots extracted from the *X*COx-25^{RH} samples: (a) *X*COx-25^{30} dry pellets; and (b) *X*COx-25^{95} wet pellets. Variation in the extracted (c) activation energies and (d) diffusion coefficients with argillite addition is also shown. liq. = liquid.

Regarding the ice part of the Arrhenius plot for this 100COx-25^{95} pellet, we visually observe an increase in the slope (directly related to an increase in E_a; Table 3), along with a loss in linearity at the lower temperatures. These observations indicate a change in the mineral matrix formed by the alkali-activated argillite, induced by storage under water-saturated conditions. Although initially this matrix had very little or no porosity, as shown by the Arrhenius plots for dry samples (Fig. 5a), new paths were created that enabled ionic conduction when stored under high-humidity conditions. A small decrease in E_a (considering the liquid state of the interstitial solution) was then measured with the addition of argillite in wet storage (~0.18 eV for the 67COx-25^{95} and 100COx-25^{95} samples compared to ~0.25 eV for the 0COx-25^{95} and 33COx-25^{95} samples). Moreover, it should be noted that sample 33COx-25^{95} seems to present these two activation energies, with an Arrhenius plot parallel to 0COx-25^{95} for $T > 290$ K and parallel to 100COx-25^{95} (or 67COx-25^{95}) for 260 K $< T <$ 290 K. This limited change in E_a is combined with a clearer variation in the diffusion coefficients, consisting of a sharp decrease at first (seven-fold reduction for 33COx-25^{95} compared to 0COx-25^{95}), followed by a strong increase (two-fold increase for 100COx-25^{95} compared to 0COx-25^{95}). This therefore calls into question the occurrence of a resumption of the alkaline activation induced by the presence of water, as had been assumed previously (Gomes *et al.*, 2021). This continuation of alkaline activation in a wet atmosphere leads to the formation of a new kind of open porous network, facilitating ionic conduction to a significant extent. The freezing temperature observed for sample 33COx-25^{95} ($T_{freeze} \approx 260$ K; Fig. 5b) supports the notion of the existence of a mesoporous network of extremely small diameter with extremely confined interstitial liquid.

As mentioned earlier for dry storage, *X*COx-25^{95} pellets ($X > 0$) present low fractal surface dimensions, particularly for mixed samples ($X = 0.33$ and 0.67; Table 2). Again, this suggests the coexistence of two distinct mineral subnetworks, each one with its own ionic conduction mechanism. It is interesting to note the increase in interface fractal dimension for the 100COx-25^{95} sample, increasing from 2.4 to 2.6 after 1 year (Table 2).

Ageing effect in a humid atmosphere: the 100COx-25^{95} sample

The Arrhenius plot of sample 100COx-25^{95} is somewhat different from all of the others due to the loss of linearity at very low temperatures ($T <$ 255 K; Fig. 5b), which can be correlated with the

https://doi.org/10.1180/clm.2026.10022 Published online by Cambridge University Press

Table 3. Values extracted from the EEC modelling of the spectra recorded on argillite-added *X*COx-T^{RH} (X = 33, 67 and 100) samples: E_a from the Arrhenius plot and the diffusion coefficient calculated at 20°C.

	E_a (eV)		
Sample	Liquid	Ice	D_{293} (cm^2 s^{-1})
33COx–25^{95}	0.21	0.95	0.12×10^{-7}
33COx–25^{30}	0.41		0.44×10^{-9}
67COx–25^{95}	0.17	1.20	0.90×10^{-7}
67COx–25^{30}	0.45		0.39×10^{-9}
67COx–100^{95}	0.20	1.22	1.11×10^{-7}
67COx–100^{30}	0.46		0.58×10^{-9}
67COx–200^{95}	0.21	1.11	0.90×10^{-7}
67COx–200^{30}	0.41		0.24×10^{-9}
67COx–450^{95}	0.18	1.14	0.55×10^{-7}
67COx–450^{30}	0.42		0.17×10^{-9}
67COx–600^{95}	0.20	1.12	$0.93\ 10^{-7}$
67COx–600^{30}	0.45		0.04×10^{-9}
67COx–900^{95}	0.35	–	0.0002×10^{-7}
67COx–900^{30}		–	–
100COx–25^{95} @ 2 months	0.16	1.38	1.80×10^{-7}
100COx–25^{95} @ 1 year	0.20	1.28 and 1.51	7.12×10^{-7}
100COx–25^{30}	0.67		0.11×10^{-9}
100COx–100^{95}	0.10	1.31	0.54×10^{-7}
100COx–100^{30}	0.64		0.01×10^{-9}
100COx–200^{95}	0.08	1.28	0.44×10^{-7}
100COx–200^{30}	0.52		0.02×10^{-9}
100COx–450^{95}	0.12	1.26	0.75×10^{-7}
100COx–450^{30}	0.39		0.01×10^{-9}
100COx–600^{95}	0.14	1.18	0.22×10^{-7}
100COx–600^{30}	0.38		0.004×10^{-9}
100COx–900^{95}	0.10	1.14	0.002×10^{-7}
100COx–900^{30}	0.42		0.0002×10^{-9}

existence of two distinct conduction paths. Indeed, the electrical response of the pure alkali-activated argillite material conserved in a humid atmosphere (100COx-25^{95} pellet) is very different from those of the other samples, particularly due to the presence of two separate capacitive arcs (Figs 6a & S3). These two capacitive reactance arcs are linked to two time constants ($\tau^{\alpha} = RC$, where τ is the time constant, α is the arc depression factor, R is the resistance and C is the capacity), each coming from its own conduction path. The first capacitive arc observed at high frequencies presents a τ_2 value of a few microseconds (as is commonly observed for all of the pellets studied here with a single capacitive arc), whereas the second capacitive arc (mid-frequencies) presents a τ_3 value of a few tenths of a millisecond, corresponding to a denser structure correlated with lower D_s values. The two conduction paths may correspond to what has been described as a polymer gel and internal pore solution by Guo *et al.* (2021) in a red mud-coal metakaolin geopolymer. Similarly to this previous study, we used an EEC with two CPEs in series (see inset in Fig. 6a). The 'first' capacitive arc (i.e. that observed for the high frequencies: 8000 Hz) corresponds to those observed in all of the samples from the present study (K^+ ionic motion through the mesoporous network of the geopolymer; i.e. internal pore conduction). The 'second' capacitive arc (i.e. observed for intermediate frequencies: 60 Hz) should correspond to more difficult ionic motion (the moderate alkaline activation of argillite; i.e. polymer gel). However, it should be noted that this second capacitive arc is highly flattened, indicating a strong deviation from the ideal Debye case for its associated conduction mechanism.

It is interesting to look at the variation in the electrical response of this 100COx-25^{95} sample stored for 1 year in a humid atmosphere (Fig. 6a). Ageing in a humid atmosphere for 1 year resulted in a better resolution of the high-frequency capacitive arc, which allowed the refinement of the two corresponding CPEs (Fig. 6b). The total impedance (Z), separated into four distinct elements, was then formulated as in Equation 9 for the 100COx-25^{95} pellet after 1 year:

$$Z(f) = R1 + \frac{R2}{R2.Q2.(j.2\pi.f)^{\alpha 2} + 1} + \frac{R3}{R3.Q3.(j.2\pi.f)^{\alpha 3} + 1} + \frac{1}{Q4.(j.2\pi.f)^{\alpha 4}} \quad (9)$$

The more defined high-frequency arc is attributed to domains where the ionic conduction is facilitated, most probably through the mesoporous network that is usually characteristic of geopolymers. This therefore reflects the resumption of alkaline activation of the argillite, leading – after a long shelf life – to a mesoporous mineral matrix of a geopolymer type. The loss of linearity observed for the 100COx-25^{95} sample below the freezing temperature in fact reflects the characterization of E_a of the first ionic conduction path observable between 269 and 259 K (1.51 eV; Fig. 6b & Table 3), and then the characterization of E_a of the second ionic conduction path observable between 247 and 243 K (1.28 eV; Fig. 6b & Table 3). The intermediate temperature, from 259 to 247 K, corresponds to the superimposition of both conduction regimes.

The pellet stored for 3 years in the 95% RH environment again exhibits an increase in the high-frequency capacitive arc, combined with increased flattening of the second contribution. However, we should note that this presence of two capacitive arcs (and consequently the loss of linearity of the Arrhenius plot below freezing temperature) was only observed for the pure argillite-activated pellets. Despite the large amount of argillite in its formulation, sample 67COx-25^{95} displayed an electrical response with a single capacitive loop, corresponding to the easiest ionic motion. The weak D_s fractal dimension of 2.3 for this 67COx-25^{95} pellet is an indication of relatively limited percolation between the two mineral subnetworks, implying different K^+ motion mechanisms.

Effect of post-synthesis thermal treatment: 67COx-T^{RH} and 100COx-T^{RH} series

The effects of a post-synthesis thermal treatment were observed for the two 67COx and 100COx formulations, and both dry and wet storage conditions were considered. All of the corresponding Arrhenius plots are shown in Fig. 7 for 67COx-T^{RH} and 100COx-T^{RH} pellets. Extracted activation energies and diffusion coefficients are listed in Table 3 and represented in Fig. S4.

When considering the dry storage of pellets (at 30% RH), it appears that an increase in the heat treatment temperature generates a reduction in the diffusion coefficient. E_a is only very slightly affected by the heat treatment for the 67COx-T^{30} series. However, we can observe a reduction in E_a from 450°C for the 100COx-T^{30} series, with values close to the geopolymer 0COx-25^{30} sample. Furthermore, it can be noted for the first time that it was possible to process the response of the pellet treated at 900°C and stored in a dry atmosphere (Fig. 7c). Although the conductivity was extremely low, we found a conduction mechanism with an E_a corresponding

https://doi.org/10.1180/clm.2026.10022 Published online by Cambridge University Press

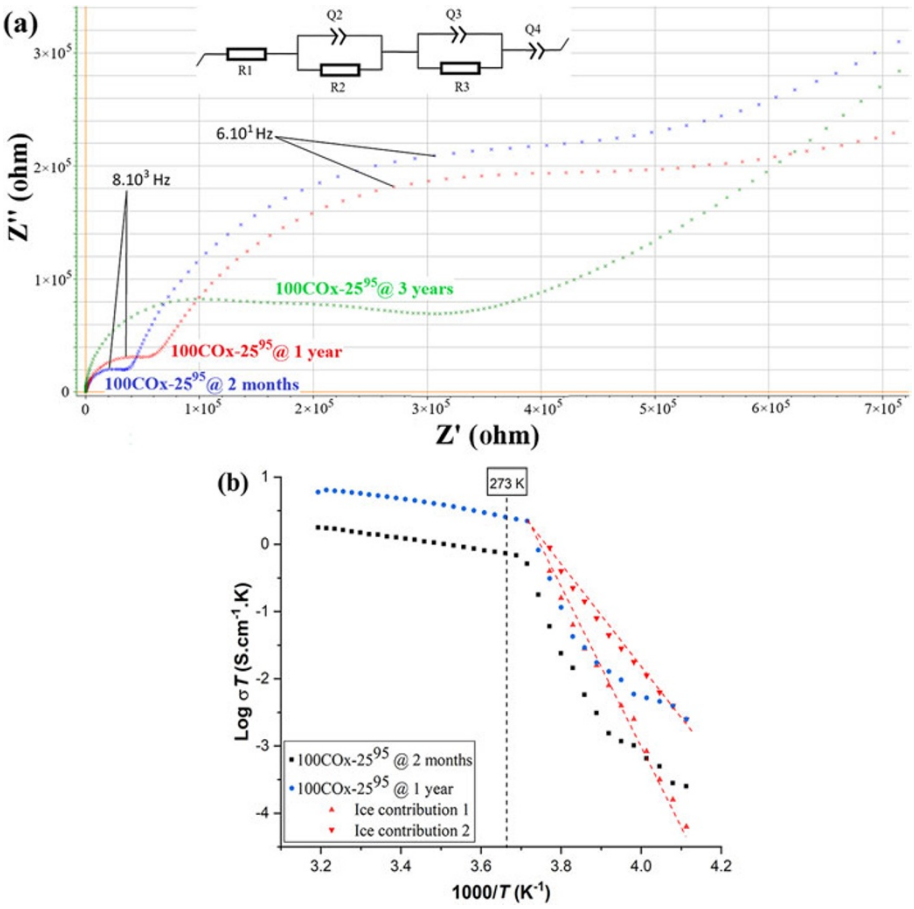


Figure 6. (a) Nyquist representations of the spectra *Z*''–*Z*' (ohm) measured at 243 K for the three 100COx-25^{95} pellets conserved for up to 3 years in a humid atmosphere. The EEC used for the impedance modelling of the spectra with two capacitive arcs is also shown. (b) Superposition of the Arrhenius plots extracted from the 100COx-25^{95} sample after 2 months and 1 year of conditioning in a humid atmosphere.

to the mesoporosity of the geopolymer. This also seemed to indicate that the heat treatment reactivated the geopolymerization process (i.e. the alkaline activation of the argillite).

Under high humidity (95% RH storage), the resumption of alkaline activation was already visible for the 67COx formulation, with an Arrhenius plot extracted from the electrical responses of the 67COx-900^{95} pellet, although no change in the physical state of the capillary liquid was detectable (due to the very small quantity of charge carriers involved). The diffusion coefficients of the 100COx series were higher than those observed for the 67COx series (Table 3 & Fig. S4). This comparison, associated with a greater E_a, indicates a more rapid frontal diffusion in the former series, but which is also more temperature-dependent than for the latter. Again, this indicates slowed and hampered conduction in the gel from the activated argillite material, which is then facilitated by the resumption of the alkaline activation initiated by the heat treatment, which then generates a more classic geopolymer mesoporous network (such as that stored in a wet atmosphere).

Discussion

All of the results obtained concerning the ionic conduction properties in our alkali-activated materials were evaluated by comparison with the previously reported results extracted from other solid characterization techniques. This allowed us, initially, to validate our interpretations of the responses of the pellets prepared and analysed using AC-IS. Thus, the results presented here subsequently enabled a complete description of the prepared alkali-activated composites, and in particular they enabled the confirmation of what had been previously and tentatively inferred without definitive experimental proof (Gomes *et al.*, 2020a, 2020b, 2021).

Open and highly traversable character of the mesoporous network

The results extracted from AC-IS analyses carried out on the pure geopolymer 0COx-25^{RH} samples are in agreement with the presence of open porosity passing through the prepared monolithic pellets. The E_a of the ionic conduction mechanism of 0.44 eV for dry atmosphere storage (0COx-25^{30} in Table 1) is in perfect agreement with the data from the literature (Melar *et al.*, 2015) and clearly indicates that the ionic conduction mechanism examined corresponds mainly to the migration of solvated K^+ cations along the mesopores characteristic of a geopolymer matrix. The filling of the mesoporosity by water in a high-humidity atmosphere only moderately facilitates ionic conduction through the pellet (E_a decreases to 0.25 eV for 0COx-25^{95}; Table 1), indicating a quite similar ionic conduction mechanism that is therefore ensured by jumps from site to site at the solid/liquid interface (i.e. at the surfaces of the mesopores). This is in agreement with residual water levels under a dry atmosphere and corresponds to a physisorbed layer on the surface of the internal porosity of the geopolymer (Gomes *et al.*, 2020a). The results for the whole 0COx-T^{RH} series agree with the thermal variation of the mesoporous network already characterized by the nitrogen adsorption isotherm and thermoporosimetry (Gomes *et al.*, 2020a, 2021), with there being almost no variation from room temperature up to 600°C, then

https://doi.org/10.1180/clm.2026.10022 Published online by Cambridge University Press

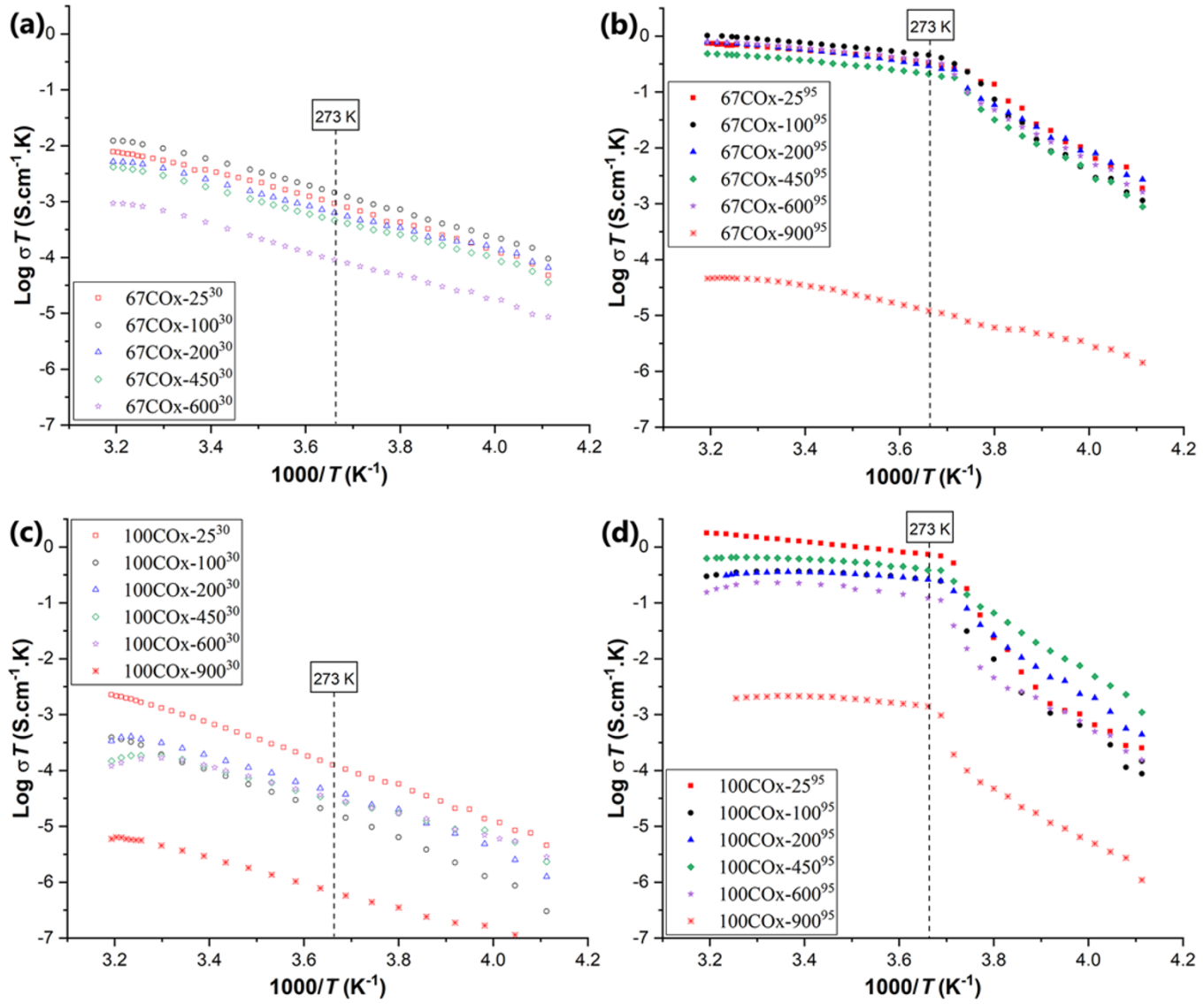


Figure 7. Superposition of the Arrhenius plots extracted from the 67COx-T^{RH} samples for (a) dry and (b) wet conditioning, and the 100COx-T^{RH} samples for (c) dry and (d) wet conditioning.

the closure of the mesoporosity at 900°C due to viscous sintering. The mesopore interface, being the location of the chemical diffusion mechanism, is relatively smooth (D_s value of ~2.6; Table 2) and changes little with the temperature.

For storage in a dry atmosphere, E_a does not show any change up to 600°C (indicating that the conduction mechanism remains the same), but the diffusion coefficient gradually decreases from 1.24×10^{-9} cm^2 s^{-1} for 0COx-25^{30} to 0.55×10^{-9} cm^2 s^{-1} for 0COx-600^{30} (Fig. 4b & Table 1). This ratio of ~2.5 corresponds to the reduction in the quantity of water physisorbed at 30% RH (13 wt.% at 25°C *vs* 5 wt.% at 600°C; see Gomes *et al.*, 2020a), thus corresponding to the water of solvation of the K^+ cations ensuring ionic conduction in these monolithic pellets. In the same way, the diffusion coefficient at 25°C and 30% RH decreases very significantly with the addition of argillite from 1.24×10^{-9} cm^2 s^{-1} for 0COx-25^{30} to 0.11×10^{-9} cm^2 s^{-1} for 100COx-25^{30} (Fig. 5d & Table 3); this must be linked to the sharp reduction in the amorphous part of the activated materials (from 99 wt.% for 0COx-25^{30} to 43 wt.% for 100COx-25^{30}), associated with a net decrease in the mesopore volume (from 0.282 cm^3 g^{-1} for 0COx-25^{30} to 0.009 cm^3 g^{-1} for 100COx-25^{30}; see Gomes *et al.*, 2021). Furthermore, the decrease in the fractal dimension of the ionic conduction interface with the addition of argillite (Table 2) indicates the coexistence of two poorly connected mineral sublattices.

K^+ location at the mesoporous interface

For the pure geopolymer 0COx-T^{RH} series, activation energies vary very little up to 600°C under both humidity storage conditions, indicating that the conduction paths are maintained (Fig. 4a & Table 1). As expressed earlier, the heat treatment followed by storage under a dry atmosphere showed a decrease in the diffusion coefficient attributed to the gradual passage of K^+ cations from the interstitial liquid to the mineral matrix in the vicinity of the

https://doi.org/10.1180/clm.2026.10022 Published online by Cambridge University Press

mesoporous interface, as already anticipated by pair distribution function analyses (Gomes *et al.*, 2020b). Regarding storage in a wet atmosphere, only the diffusion coefficient at 600°C showed a sharp decrease (from 0.85×10^{-7} cm^2 s^{-1} for 0COx-25^{95} to 0.11×10^{-7} cm^2 s^{-1} for 0COx-600^{95}; i.e. no loss of charge carriers was observed up to 450°C, still being 0.79×10^{-7} cm^2 s^{-1} for 0COx-450^{95}). These results for the 0COx-T^{95} series indicate the return of the K^+ solvated cations into the mesopore liquid cavities in the case of wet storage, except in the case of excessive heat treatment. We thus have confirmation of the reversibility (for moderate temperatures) of K^+ cation diffusion, which had also been anticipated previously (Gomes *et al.*, 2020b). This reversibility was also observed when considering D_s values for wet storage (0COx-T^{95} series; Table 2), which change little up to 450°C before decreasing at 600°C, whereas the D_s decrease was notable already at 100°C for storage in a dry atmosphere.

Presence of two distinct polymeric mineral submatrices

The Arrhenius plot of the 33COx-25^{95} pellet (Fig. 5b) presents two interesting outcomes: (1) the very low freezing temperature, certainly indicating the presence of a gel-type matrix that is different from the characteristic mesoporous matrix for a pure geopolymer; and (2) a broken-type plot in the liquid state. The linear fit for E_a^{95}(liquid) for the 33COx-25^{95} pellet gives a value of 0.21 eV, which is the mean value between 0.25 eV for the 0COx-25^{95} pellet and 0.17 eV for the 67COx-25^{95} pellet. In fact, we first observe linear behaviour between 263 and 287 K, with a slope corresponding to an E_a value of 0.17 eV, then a second linear section above 287 K, with a slope corresponding to an E_a value of 0.25 eV. These two activation energies at 25°C should correspond to two distinct conduction paths, each characterizing a domain within which ionic conduction is permitted. The E_a value of 0.25 eV is then characteristic of the mesopores intrinsic to the geopolymer matrix resulting from the alkaline activation of a metakaolin. It follows that the E_a value of 0.17 eV should be characteristic of the mineral matrix obtained by the alkaline activation of the argillite, which also enables ionic mobility through a different path/domain.

It should be noted that the E_a variation for the series *X*COx-25^{95} when considering the freezing state (labelled E_a^{95}(ice) in Fig. 5c) shows the opposite trend, being higher for an argillite-activated material compared to a pure geopolymer. In the same way, the storing of these compositions under dry conditions (i.e. the *X*COx-25^{30} pellets) induced an increase in E_a^{30} for the pure alkali-activated argillite material (0.67 eV for 100COx-25^{30} *vs* ~0.45 eV for the other compositions; Fig. 5c & Table 3). These opposite variations, although of the same order, between E_a in the liquid state (E_a^{95}(liquid)) and in the 'dry' state (E_a^{30} and E_a^{95}(ice)) as a function of the argillite amount must indicate that ionic conductions through the geopolymer matrix and through the argillite-activated matrix are both provided by the same ionic species (solvated K^+) using surface sites that describe different interfaces, therefore crossing two different and poorly connected polymeric mineral matrices.

An additional confirmation of the existence of these two distinct amorphous mineral domains was provided by the 100COx-25^{95} pellet, which indicated a two-path mechanism for ionic conduction at low temperatures (i.e. below the freezing temperature). This double conduction path was clearly identifiable by the presence of two capacitive arcs identified in its electrical responses (Figs 6 & S3). Two activation energies could be determined from these spectra refinements (Fig. 6b & Table 3): one of 1.28 eV, corresponding to the ionic conduction path through the geopolymer matrix, and the other of 1.51 eV, which should be attributed to the argillite-activated gel. The coexistence of two amorphous mineral subnetworks has already been indicated for geopolymers loaded with C-type (calcium-containing) fly ashes leading to the formation of C-S-H gels intimately mixed within the geopolymer matrix (Bai *et al.*, 2023).

Resumption of argillite alkaline activation

A supplementary experimental proof of the existence of an argillite-activated gel, which should be differentiated from the purely mesoporous geopolymer matrix, is the resumption of argillite alkaline activation, initiated either by thermal treatment or more effectively by long-term conditioning in a humid atmosphere. This resumption of argillite activation had already been supposed in a previous study from nitrogen isotherm adsorption results (Gomes *et al.*, 2021). The most explicit experimental result on this topic is the time-dependent variation in the electrical response for the 100COx-25^{95} pellet, which was even more pronounced with long-time storage (Fig. 6). The two capacitive arcs are representative of two conduction paths already being present after 2 months. Over time, the subnetwork attributed to argillite alkaline activation is replaced by a geopolymer-type network with a smoother ideal interface. This means that the resumption of alkaline activation in humid conditions favours the formation of a mesopore network that is topologically similar to that present in a pure geopolymer coming from the activation of a reactive metakaolin. Finally, the decrease in E_a in the 100COx-T^{30} and 100COx-T^{95} series (Table 3 & Fig. S4b) with temperature is also an indication of the fact that this resumption of the alkaline activation of argillite is thermally facilitated.

Conclusion

The study presented here enabled us, as a first step, to validate the AC-IS method for the fine characterization of the mesoporous network features of geopolymers. The relatively simple nature of these mesoporous networks enables the use of a simple and robust EEC model and consequently the interpretation of values extracted from this electrical model in physico-chemical characterizations of the material. The main results of this study have experimentally confirmed previously formulated hypotheses.

The presence of a single conduction path is related to the description of an open and homogeneous mesoporosity that crosses the material from one side to the other following the activation of a reactive metakaolin. Considering that ionic conduction is mainly attributed to K^+ cations, it was possible to locate these cations in the interstitial liquid (therefore being solvated) of the synthesized geopolymer. It was shown that these cations diffused into the mineral matrix during heat treatment. This diffusion is reversible for moderate temperatures (up to 450°C) in the case of subsequent exposure to high RH.

The presence of argillite, being less reactive than metakaolin, generates a gel with a different microstructure from that of a typical geopolymer, and so this induces a different ionic conduction mode (one that is more difficult but with a larger number of charge carriers). This gel network will be able to evolve over the long term when exposed to a wet atmosphere and also under moderate temperatures, resulting in a mesoporous network whose characteristics are close to those of pure geopolymers.

https://doi.org/10.1180/clm.2026.10022 Published online by Cambridge University Press

Supplementary material. The supplementary material for this article can be found at https://doi.org/10.1180/clm.2026.10022.

Financial support. This project was supported by Andra under the 'Investments for the Future' programme; selected under the Andra Call for Projects: 'Optimisation of post-dismantling radioactive waste management', organized in cooperation with the French National Research Agency (ANR).

Competing interests. The authors declare none.

References

Babushkin V., Matveyev G. & Mchedlov-Petrossyan O. (1985) *Thermodynamics of Silicates*. Springer-Verlag, Berlin, Germany, 459 pp.

Bai B., Bai F., Nie Q. & Jia X. (2023) A high-strength red mud-fly ash geopolymer and the implication of curing temperature. *Powder Technology*, **416**, 118242.

Bai B., Wu H., Nie Q., Liu J & Jia X. (2025a) Granular thermodynamic migration model suitable for high-alkalinity red mud filtrates and test verification. *International Journal of Numerical and Analytic Methods in Geomechanics*, **49**, 1530–1543.

Bai B., Wu H. Zhou R., Wu N. & Zhang B. (2025b) A granular thermodynamic framework-based coupled multiphase-substance flow model considering temperature driving effect. *Journal of Rock Mechanics and Geotechnical Engineering*, **17**, 5816–5828.

Barbosa V.F.F. & MacKenzie K.J.D. (2003) Thermal behaviour of inorganic geopolymers and composites derived from sodium polysialate. *Materials Research Bulletin*, **38**, 319–331.

Biondi L., Perry M., McAlorum J., Vlachakis C. & Hamilton A. (2020) Geopolymer-based moisture sensors for reinforced concrete health monitoring, *Sensors and Actuators B: Chemical*, **309**, 127775.

Cabeza M., Merino P., Miranda A., Novoa X.R. & Sanchez I. (2002) Impedance spectroscopy study of hardened Portland cement paste. *Cement and Concrete Research*, **32**, 881–891.

Cabeza M., Keddam M., Novoa X.R., Sanchez I. & Takenouti H. (2006) Impedance spectroscopy to characterize the pore structure during the hardening process of Portland cement paste. *Electrochimica Acta*, **51**, 1831–1841.

Cantarel V., Nouaille F., Rooses A., Lambertin D., Poulesquen A. & Frizon F. (2015) Solidification/stabilisation of liquid oil waste in metakaolin-based geopolymer. *Journal of Nuclear Materials*, **464**, 16–19.

Chi L., Wang Z., Lu S., Zhao D. & Yao Y. (2019) Development of mathematical models for predicting the compressive strength and hydration process using the EIS impedance of cementitious materials. *Construction and Building Materials*, **208**, 659–668.

Chlique C., Lambertin D., Antonucci P., Frizon F. & Deniard P (2015) XRD analysis of the role of cesium in sodium-based geopolymer. *Journal of the American Ceramics Society*, **98**, 1308–1313.

Cormack S.L., McPhee D.E. & Sinclair D.C. (1998) An AC impedance spectroscopy study of hydrated cement pastes. *Advances in Cement Research*, **10**, 151–159.

Cruz J.M., Fita I.C., Soriano L., Paya J. & Borrachero M.V. (2013) The use of electrical impedance spectroscopy for monitoring the hydration products of Portland cement mortars with high percentage of pozzolan. *Cement and Concrete Research*, **50**, 51–61.

Da Silva G.F., Martini S., Moraes J.C.B. & Teles L.K. (2021) AC impedance spectroscopy (AC-IS) analysis to characterize the effect of nanomaterials in cement-based mortars. *Construction and Building Materials*, **269**, 121260.

Dimas D., Giannopoulou I. & Panias D. (2009) Polymerization in sodium silicate solutions: a fundamental process in geopolymerization technology. *Journal of Materials Science*, **44**, 3719–3730.

Dong B., Qiu Q., Xiang J., Huang C., Xing F., Han N. & Lu Y. (2014) Electrochemical impedance measurement and modeling analysis of the carbonation behavior for cementitious materials. *Construction and Building Materials*, **54**, 558–565.

Dupuy C., Gharzouni A., Teixier-Mandoki N., Bourbon X. & Rossignol S. (2018) Alkali-activated materials based on Callovo-Oxfordian argillite: formation, structure, and mechanical properties. *Journal of Ceramic Science and Technology*, **9**, 127–140.

Duxson P., Fernández-Jiménez A., Provis J.L., Lukey G.C., Palomo A. & van Demeter J.S.J. (2007a) Geopolymer technology: the current state of the art. *Journal of Materials Science*, **42**, 2917–2933.

Duxson P., Provis J.L., Lukey G.C. & van Deventer J.S.J. (2007b) The role of inorganic polymer technology in the development of 'green concrete. *Cement and Concrete Research*, **37**, 1590–1597.

Fernández-Jiménez A., Palomo A., Pastor J.Y. & Martin A. (2008) New cementitious materials based on alkali activated fly ash: performance at high temperatures. *Journal of the American Ceramics Society*, **91**, 3308–3314.

Ford S.J., Hwang J.H., Shane I.D., Olson R.A., Moss G.M., Jennings H.M. & Mason T.O. (1997) Dielectric amplification in cement pastes. *Advanced Cement Based Materials*, **5**, 41–48.

Gharzouni A., Dupuy C., Sobrados I., Joussein E., Teixier-Mandoki N., Bourbon X. & Rossignol S. (2017) The effect of furnace and flash heating on COx argillite for the synthesis of alkali-activated binders. *Journal of Cleaner Production*, **156**, 670–678.

Gomes S., Petit E., Frezet L., Nedelec J.M., Gharzouni A., Rossignol S. & Renaudin G. (2020a) Temperature stability of a pure metakaolin K-geopolymer: part 2. Variations in the mesoporous network and its rehydration ability. *Journal of the American Ceramics Society*, **103**, 5813–5824.

Gomes S., Petit E., Frezet L., Thirouard R., Taviot-Gueho C., Gharzouni A. *et al*. (2020b) Temperature stability of a pure metakaolin K-geopolymer: part 1. Variations in the amorphous mineral network. *Journal of the American Ceramics Society*, **103**, 5914–5926.

Gomes S., Frezet L., Petit E., Petlickaia S., Rossignol S., Texier-Mandoki N. & Renaudin G. (2021) Temperature stability of an argillite/K-geopolymer composite: impact of argillite filler on dimensional behavior. *Open Ceramics*, **5**, 100081.

Grammatikos S.A., Ball R.J., Evernden M. & Jones R.G. (2018) Impedance spectroscopy as a tool for moisture monitoring in construction composite during service. *Composites: Part A*, **105**, 108–117.

Gu P., Xie P., Beaudoin J.J. & Brousseau R. (1992) AC impedance spectroscopy (I): a new equivalent circuit model for hydrated Portland cement paste. *Cement and Concrete Research*, **22**, 833–840.

Gui Q., Qin M. & Li K. (2016) Gas permeability and electrical conductivity of structural concretes: impact of pore structure and pore saturation. *Cement and Concrete Research*, **89**, 109–119.

Guo T., Wu T., Gao L., He B., Ma F., Huang Z. & Bai X. (2021) Compressive strength and electrochemical impedance response of red mud–coal metakaolin geopolymer exposed to sulfuric acid, *Construction and Building Materials*, **303**, 124523.

Habert G. & Ouellet-Plamondon C. (2016) Recent update on the environmental impact of geopolymers. *RILEM Technical Letters*, **1**, 17–23.

Imre A., Pajkossy T. & Nyikos L. (1992) Electrochemical determination of the fractal dimension of fractured surfaces. *Acta Metallurgica et Materialia*, **40**, 1819–1826.

Keddam M., Takenouti H., Novoa X.R., Andrade C. & Alonso C. (1997) Impedance measurements on cement paste. *Cement and Concrete Research*, **27**, 1191–1201.

Kong D.L.Y., Sanjayan J.G. & Sagoe-Crentsil K. (2007) Comparative performance of geopolymers made with metakaolin and fly ash after exposure to elevated temperatures. *Cement and Concrete Research*, **37**, 1583–1589.

Kriven W.M., Bell J.L. & Gordon M. (2007) Microstructure and nanoporosity of as-set geopolymers. *Ceramic Engineering and Science Proceedings*, **27**, 491–503.

Lambertin D., Frizon F., Blachere A. & Bart F. (2011) Corrosion behaviour of Mg alloys in various basic media: application of waste encapsulation of fuel decanning from UNGG nuclear reactor. Pp. 435–439 in: *Magnesium Technology* (W.H. Sillekens, S.R. Agnew, N.R. Neelameggham & S.N. Mathaudhu, editors). Springer, Cham, Switzerland.

Leroux F., Russias J., Cau-dit-Coumes C., Frizon F. & Renaudin G. (2011) Low-to-medium frequency AC impedance spectroscopy investigation of nanocrystalline calcium silicate hydrate dried powders. *Journal of the American Ceramics Society*, **94**, 2680–2687.

Li W., Ji W., Fang G., Liu Y., Xing F., Liu Y. & Dong B. (2016) Electrochemical impedance interpretation for the fracture toughness of

carbon nanotube/cement composite. *Construction and Building Materials*, **114**, 499–505.

Li Z., Chen R. & Zhang L.Y. (2013) Utilization of chitosan biopolymer to enhance fly ash-based geopolymer. *Journal of Materials Science*, **48**, 7986–7993.

Liu J., Lu Y., Bai X., Han P., Xie R. & He B. (2020) Strength characteristics and electrochemical impedance spectroscopy characterization of red mud–coal metakaolin geopolymer. *International Journal of Electrochemical Science*, **15**, 10694–10706.

Long Q., Yan H., Wu H., Qiu S., Zhou X. & Qiu T. (2025) Influence mechanism of leaching agent anions on the leaching of aluminium impurities in ionic-type rare earth ores: a DFT simulation combined with experimental verification. *Separation and Purification Technology*, **354**, 128768.

Malviya M. & Goliya H. (2014) Durability of fly ash based geopolymer concrete using alkaline solutions (NaOH and Na_2SiO_3). *International Journal of Emerging Trends in Engineering and Technology*, **6**, 18–33.

Massey S.W. (1996) Application of fractal geometry and electrical impedance measurement for the assessment of strength of granular materials. *Building and Environment*, **31**, 493–501.

McCarter W.J. (1994) A parametric study of the impedance characteristic of cement aggregate systems during early hydration. *Cement and Concrete Research*, **24**, 1097–1110.

McCarter W.J. & Garvin S. (1989) Dependence of electrical impedance of cement-based materials on their moisture condition. *Journal of Physics D: Applied Physics*, **22**, 1773–1776.

McLellan B.C., Williams R.P., Lay J., van Riessen A. & Corder G.D. (2011) Costs and carbon emissions for geopolymer pastes in comparison to ordinary Portland cement. *Journal of Cleaner Production*, **19**, 1080–1090.

McPhee D.E., Sinclair D.C. & Stubbs S.L. (1996) Electrical characterization of pore reduced cement by impedance spectroscopy. *Journal of Materials Science Letters*, **15**, 1566–1568.

McPhee D.E., Sinclair D.C. & Cormack S.L. (1997) Development of an equivalent circuit model for cement paste from microstructure considerations. *Journal of the American Ceramics Society*, **80**, 2876–2884.

Melar J., Renaudin G., Leroux F., Hardy-Dessources A., Nedelec J.M., Taviot-Gueho C. *et al*. (2015) The porous network and its interface inside geopolymers as a function of alkali cation and aging. *Journal of Physical Chemistry C*, **119**, 17619–17632.

Melara E.K., Mendes A.Z., Andreczevecz N.C., Braganca M.O.G.P., Carrera G.T. & Medeiros-Junior R.A. (2020) Monitoring by electrochemical impedance spectroscopy of mortars subjected to ingress and extraction of chloride ions. *Construction and Building Materials*, **242**, 118001.

Mendes S.E.S., Oliveira R.L.N., Cremonez C., Pereira E., Pereira E. & Medeiros-Junior R.A. (2018) Electrical resistivity as a durability parameter for concrete design: experimental data versus estimation by mathematical model. *Construction and Building Materials*, **192**, 610–620.

Moss G.M., Christensen B.J., Mason T.O. & Jennings H.M. (1996) Microstructural analysis of young cement paste using impedance spectroscopy during pore solution exchange. *Advanced Cement Based Materials*, **4**, 68–75.

Nyikos L. & Pajkossy T. (1985) Fractal dimension and fractional power frequency-dependent impedance of blocking electrodes. *Electrochimica Acta*, **30**, 1533–1540.

Ortega J.M., Sanchez I. & Climent M.A. (2015) Impedance spectroscopy study of the effect of environmental conditions in the microstructure development of OPC and slag cement mortars. *Archives of Civil and Mechanical Engineering*, **15**, 569–583.

Pacheco-Torgal F., Castro-Gomes J.P. & Jalali S. (2006) Bond strength between concrete substance and repair materials: comparisons between tungsten mine waste geopolymeric binder versus current commercial repair products. Presented at: *7th International Congress on Advances in Civil Engineering*, Istanbul, Turkey.

Pacheco-Torgal F., Abdollahnejad Z., Camões A.F., Jamshidi M. & Ding Y. (2012) Durability of alkali-activated binders: a clear advantage over Portland cement or an unproven issue? *Construction and Building Materials*, **30**, 400–405.

Palomo A. & Lopez de la Fuente J.I. (2003) Alkali-activated cementitous materials: alternative matrices for the immobilisation of hazardous wastes: part I. Stabilisation of boron. *Cement and Concrete Research*, **33**, 281–288.

Palomo A., Blanco-Valera M.T., Granizo M.L., Puertas F., Vazquez T. & Grutzeck M.W. (1999) Chemical stability of cementitious materials based on metakaolin. *Cement and Concrete Research*, **29**, 997–1004.

Provis J.L. & van Deventer J.S.J. (editors) (2009) *Geopolymers: Structures, Processing, Properties and Industrial Applications*. Woodhead Publishing, Abingdon, UK, 454 pp.

Provis J.L., Duxson P., van Demeter J.S.J. & Lukey G.C. (2005) The role of mathematical modelling and gel chemistry in advancing geopolymer technology. *Chemical Engineering Research and Design*, **83**, 853–860.

Risovic D., Mahovic Poljacek S., Furic K. & Gojo M. (2008) Inferring fractal dimension of rough/porous surface – a comparison of SEM image analysis and electrochemical impedance spectroscopy methods. *Applied Surface Science*, **255**, 3063–3070.

Sanish K.B., Neithalath N. & Santhanam M. (2013) Monitoring the evolution of material structure in cement pastes and concretes using electrical property measurements. *Construction and Building Materials*, **49**, 288–297.

Sengul O. (2014) Use of electrical resistivity as an indicator for durability. *Construction and Building Materials*, **73**, 434–441.

Shen P., Han P., Guo T., Wang R., Song W., Bai X. *et al*. (2022) Study on the setting and hardening process of a red mud–coal metakaolin geopolymer concrete by electrochemical impedance spectroscopy. *International Journal of Electrochemical Science*, **17**, 221158.

Song G. (2000) Equivalent circuit model for AC electrochemical impedance spectroscopy of concrete. *Cement and Concrete Research*, **30**, 1723–1730.

Song Q., Wang J., Dong T., He L. & Lu S. (2019) Study of the alkali activated geopolymer by AC impedance spectroscopy. *IOP Conference Series: Earth and Environmental Science*, **267**, 022001.

Tang S.W., Li Z.J., Shao H.Y. & Chen E. (2014) Characterization of early-age hydration process of cement pastes based on impedance measurement. *Construction and Building Materials*, **68**, 491–500.

Tang S.W., Cai X.H., He Z., Zhou W., Shao H.Y., Li Z.J. *et al*. (2016) The review of pore structure evaluation in cementitious materials by electrical methods. *Construction and Building Materials*, **117**, 273–284.

Wang R., He F., Shi C., Zhang D., Chen C. & Dai L. (2022) AC impedance spectroscopy of cement-based materials: measurement and interpretation. *Cement and Concrete Composites*, **131**, 104591.

Weil M., Dombrowski K. & Buchwald A. (2009) Geopolymers. Pp. 194–210 in: *Life-Cycle Analysis of Geopolymers*. Woodhead Publishing, Abingdon, UK.

Xia Y., Wei W., Liu Y., Cai Z., Zhang Q. & Cai J. (2021) A fractal-based approach to evaluate the effect of microstructure on the permeability of two-dimensional porous media. *Applied Geochemistry*, **131**, 105013.

Xie P., Gu P. & Beaudoin J.J. (1993) A rationalized A.C. impedance model for microstructure characterization of hydrating cement systems. *Cement and Concrete Research*, **23**, 359–367.

Xu H. & van Deventer J.S.J. (2000) The geopolymerisation of alumino-silicate minerals. *International Journal of Mineral Processing*, **59**, 247–266.

Zhang S., Tan D., Zhu H., Pei H. & Shi B. (2025) Rheological behaviors of Na-montmorillonite considering particle interactions: a molecular dynamic study. *Journal of Rock Mechanics and Geotechnical Engineering*, **17**, 4657–4671.

https://doi.org/10.1180/clm.2026.10022 Published online by Cambridge University Press